Published in final edited form as:
ChemCatChem. ; 16(11): . doi:10.1002/cctc.202301218.

Synergistic Effects of Silica-Supported Iron–Cobalt Catalysts for CO_2 Reduction to Prebiotic Organics

Dr. Kendra S. Belthle[a], **Prof. Dr. William F. Martin**[b], **Dr. Harun Tüysüz**[a]
[a]Max-Planck-Institut für Kohlenforschung, Kaiser-Wilhelm-Platz 1, , 45470, Mülheim an der Ruhr, Germany.

[b]Institute of Molecular Evolution, University of Düsseldorf, Universitätsstraße 1, 40225 Düsseldorf, Germany

Abstract

To test the ability of geochemical surfaces in serpentinizing hydrothermal systems to catalyze reactions from which metabolism arose, we investigated H_2-dependent CO_2 reduction toward metabolic intermediates over silica-supported Co−Fe catalysts. Supported catalysts converted CO_2 to various products at 180 °C and 2.0 MPa. The liquid product phase included formate, acetate, and ethanol, while the gaseous product phase consisted of CH_4, CO, methanol, and C_2−C_7 linear hydrocarbons. The 1/1 ratio CoFe alloy with the same composition as the natural mineral wairauite yielded the highest concentrations of formate (6.0 mM) and acetate (0.8 mM), which are key intermediates in the acetyl-coenzyme A (acetyl-CoA) pathway of CO_2 fixation. While Co-rich catalysts were proficient at hydrogenation, yielding mostly CH_4, Fe-rich catalysts favored the formation of CO and methanol. Mechanistic studies indicated intermediate hydrogenation and C−C coupling activities of alloyed CoFe, in contrast to physical mixtures of both metals. Co in the active site of Co−Fe catalysts performed a similar reaction as tetrapyrrole-coordinated Co in the corrinoid iron-sulfur (CoFeS) methyl transferase in the acetyl-CoA pathway. In a temperature range characteristic for deeper regions of serpentinizing systems, oxygenate product formation was favored at lower, more biocompatible temperatures.

Keywords

Heterogeneous catalysis; Prebiotic Chemistry; Hydrothermal Vent; CO_2 Fixation; CoFe Alloy

1 Introduction

Life’s origin on the early Earth required a continuous supply of partially reduced organic carbon compounds from which metabolism and cells arose. Proposals for that supply

---

Correspondence to: Harun Tüysüz.

tueysuez@kofo.mpg.de .

Conflict of Interests
The authors declare no conflict of interest.

include ‘primordial soup’,[1,2] extraterrestrial delivery of organic molecules,[3–5] and surface metabolism by CO_2 fixation in hydrothermal vents.[6,7] The latter interfaces well with the chemistry of modern cells because hydrothermal vents harbor rich ecosystems and unique geochemistry that yield organic compounds, such as formate, CH_4, and short-chain hydrocarbons, from CO_2 reduction.[8–12] The H_2 required for CO_2 reduction is supplied by a reaction called serpentinization, in which Fe(II)-containing minerals in ultramafic rocks are oxidized by seawater, generating as products Fe(III)-minerals and H_2 gas, a powerful and diffusible reductant capable of reducing CO_2 under geochemical conditions.[13,14] In the presence of up to 16 mmol H_2/kg of vent effluent, zero-valent transition metals can also be formed in serpentinized ultramafic rocks, including metallic iron, cobalt, nickel, and their alloys, such as awaruite (Ni_3Fe) and wairauite (CoFe).[13,15–17] These minerals are considered as possible prebiotic catalysts for the H_2-dependent CO_2 fixation, the geochemical ancestors of enzymes and cofactors in the biochemical acetyl-coenzyme A (acetyl-CoA) pathway of carbon metabolism.[18] Being ancient and the only exergonic pathway of autotrophic carbon metabolism, it is still the backbone of carbon and energy metabolism in modern acetogens and methanogens, its enzymes and cofactors contain the same transition metals in their active centers as found at hydrothermal vents.[19–21]

Typical heterogeneous catalysts for CO and CO_2 hydrogenation to value-added products are based on Fe and Co metals.[22,23] As summarized in equations (1)–(4), the main industrial reactions involved in CO_2 hydrogenation include reverse water-gas shift reaction (RWGS) toward CO, the Sabatier reaction for CO_2 methanation, methanol synthesis, and hydrocarbon formation.[24]

$$\begin{gathered}\text{RWGS}: \\ \mathrm{CO_2(g)} + \mathrm{H_2(g)} \rightarrow \mathrm{CO(g)} + \mathrm{H_2O(g)}, \\ \Delta H^0{}_{298K} = +41.2\ \mathrm{kJmol^{-1}}\end{gathered} \tag{1}$$

$$\begin{gathered}\text{Methanation}: \\ \mathrm{CO_2(g)} + 4\mathrm{H_2(g)} \rightarrow \mathrm{CH_4(g)} + 2\mathrm{H_2O(g)}, \\ \Delta H^0{}_{298K} = -164.7\ \mathrm{kJmol^{-1}}\end{gathered} \tag{2}$$

$$\begin{gathered}\text{Methanol synthesis}: \\ \mathrm{CO_2(g)} + 3\mathrm{H_2(g)} \rightarrow \mathrm{CH_3OH(g)} + \mathrm{H_2O(g)}, \\ \Delta H^0{}_{298K} = -49.3\ \mathrm{kJmol^{-1}}\end{gathered} \tag{3}$$

$$\begin{gathered}\text{RWGS} + \text{FTS}: \\ n\mathrm{CO_2(g)} + (3n+1)\mathrm{H_2(g)} \rightarrow \mathrm{C}_n H_{2n+2}(\mathrm{g, I}) + 2n\mathrm{H_2O(g)}\end{gathered} \tag{4}$$

Among those reactions, methanol synthesis and methanation are exothermic, while RWGS is endothermic and thermodynamically favorable at higher temperatures. For the formation of hydrocarbons, typically a combination of RWGS for CO generation and Fischer-Tropsch synthesis (FTS) for C−C coupling is proposed. This was found to be promoted over Co−Fe bimetallic catalysts compared to the monometallic counterparts.[25,26] Similarly, the formation of higher alcohols is possible but even more challenging due to the requirement of active sites capable of associative and dissociative activation of CO intermediates for C−C coupling.[27] Also acetic acid formation with Co−Fe bimetallic catalysts has been reported but controlling the hydrogenation ability by K-promotion was found to be crucial to prevent further reduction toward the alcohol.[28]

Studies on CO_2 fixation to prebiotic organic carbon compounds under hydrothermal vent conditions modeled in the laboratory, on the other hand, have so far mostly focused on Fe- and Ni-based catalysts and yielded a product spectrum including formate, acetate, and pyruvate in mM range together with methanol, and CH_4.[29–36] However, also Co plays a central role in the methyl biochemistry for acetyl synthesis via the acetyl-CoA pathway. The transfer of a pterin-bound methyl group to a nickel atom in the active site of the enzyme acetyl-CoA synthase for carbonyl insertion by CO occurs via the tetrapyrrole-coordinated Co in an ancient methyl transferase, the corrinoid iron-sulfur (CoFeS) protein.[20,37] In a previous study, we demonstrated the ability of silica-supported Co-based catalysts to reduce CO_2 to metabolic intermediates like formate and acetate in presence of H_2.[38] In a study by He et al., the combination of Co and Fe metals for carbon reduction was investigated using bicarbonate as the carbon source.[39] With a physical mixture of both metals, they reported a possible mechanism for long-chain hydrocarbon formation up to C_{24} at hydrothermal vents accompanied by the formation of formate under harsh conditions of 300 °C and 30 MPa. Recently, Peters et al. demonstrated the ability of supported meteoritic and volcanic particles to catalyze CO_2 reduction to hydrocarbons, methanol, ethanol, formaldehyde, and acetaldehyde over a broad plausible temperature and pressure range for the early Earth. The Fe-rich catalysts partly contained additional Ni and Co metals, but only in amounts of <1 wt% in case of the latter.[40] Synergistic effects of alloying of Fe and Co metals in equimolar ratios as in the natural mineral wairauite have not been addressed.

Here, we systematically investigate bimetallic of alloyed Co−Fe catalysts in H_2-dependent CO_2 reduction to prebiotic carbon compounds under plausible hydrothermal vent conditions. The use of a mesoporous silica support further simulates the silica-rich environment of surrounding minerals.[41] Also, internal porosity forming prebiotic micro spaces is thought to sufficiently concentrate the organic building blocks for finally starting a self-replicating system in hydrothermal vents.[18] The effects of the Fe/Co ratio and reaction temperature on activity and selectivity in CO_2 hydrogenation are systematically investigated. Different analytic techniques including reactant sorption studies together with variations in the catalyst contact time are further employed to propose a reaction mechanism.

Exerimental Section

Materials

Cobalt(II) nitrate hexahydrate ($Co(NO_3)_2 \cdot 6H_2O$; ACS reagent grade 99.5 %, Sigma-Aldrich), iron(III) nitrate nonahydrate ($Fe(NO_3)_3 \cdot 9H_2O$; ACS reagent grade ≥98%, Sigma-Aldrich), and silica gel (Davisil Grade 62, high-purity grade, pore size 150 Å, 60–200 mesh, Supelco) were used as purchased.

Catalyst Synthesis

Silica-supported Co−Fe catalysts with varying atomic ratios (Co, Co_3Fe, Co_5Fe_3, CoFe, Co_3Fe_5, $CoFe_3$, and Fe) were synthesized by a wet impregnation method. The total molar metal amount was fixed for all catalysts and the loading was ~15 wt % of metal on support weight basis. Typically, 3 g of the silica gel support material was dispersed in a solution of 8 mmol metal nitrate salt in 30 mL of EtOH and stirred for 2 h at room temperature. Subsequently, the impregnated support was dried at 45 °C in air overnight, followed by calcination in static air at 400 °C for 4 h (2 °C min^{-1}). Reduction of the supported mixed metal oxides was performed at 450 °C for 8 h in 100 cm^3 min^{-1} H_2 flow (1 °C min^{-1}). Subsequent surface passivation of the metallic nanoparticles for 2 h in 90 cm^3 min^{-1} Ar/10 cm^3 min^{-1} synthetic air flow prevented unregulated oxidation upon exposure to air.

Catalyst Characterization

Powder X-ray diffraction (XRD) patterns were collected in Bragg–Brentano geometry using a PANalytical X'Pert Pro diffractometer with a Cu Kα radiation source at room temperature. The instrument was equipped with a Kβ filter and a RTMS X'Celerator Scientific detector. Data were collected between 10 and 80° 2θ with a step width of 0.0167° 2θ and 100 s measuring time per step. For each sample ten scans were collected and summed up.

Metal loadings were determined by bulk scanning electron microscopy coupled with energy dispersive X-ray spectroscopy (SEM-EDX) in a Hitachi S-3500 N equipped with a Si(Li) Pentafet plus detector from Oxford Instruments operated at 30 kV.

Bright-field images of the catalysts were collected with a transmission electron microscope (TEM) Hitachi H7500 equipped with a LaB_6 field emission electron source and operated at 100 kV acceleration voltage. High-resolution scanning transmission electron microscopy (HR–STEM) and high-angle annular dark-field (HAADF) imaging coupled with EDX was performed with a Thermo Scientific Talos F200× (S)TEM microscope equipped with a SuperX EDS system at an acceleration voltage of 200 kV.

Different types of chemisorption experiments were performed in a Micromeritics AutoChem II 2920. Hydrogen temperature-programmed reduction (H_2-TPR) experiments were performed with about 60 mg of the calcined-supported metal oxides. Firstly, the catalysts were pretreated at 200 °C in 50 cm^3 min^{-1} He flow for 60 min (10 °C min^{-1}). After cooling down to 45 °C at 5 °C min^{-1}, the gas flow was switched to 10 vol% H_2 in Ar (50 cm^3 min^{-1}). Then, the H_2 consumption rate was monitored by a thermal conductivity detector

(TCD) while increasing the temperature to 1000 °C at a heating rate of 10 °C min^{-1}. The generated water during the reduction was retained by an acetone/dry ice trap.

In temperature-programmed desorption of hydrogen (H_2-TPD), about 60 mg of the reduced Co−Fe catalysts were treated at 450 °C for 1.5 h (5 °C min^{-1}) in 10% H_2/Ar flow (50 cm^3 min^{-1}) to reduce the surface passivation layer and an acetone/dry ice trap was used to retain any formed water. After cooling down to 40 °C (10 °C min^{-1}), the sample tube was flushed with Ar (25 cm^3 min^{-1}) for 65 min to remove weakly adsorbed H_2. Subsequently, the H_2 desorption profile was tracked by an online quadrupole mass spectrometer (QMS) Pfeiffer Vacuum GSD 350 Omnistar at $m/z=2$ while heating to 800 °C (10 °C min^{-1}).

Nitrogen physisorption analysis was carried out on a Micrometrics 3Flex at −196 °C. Prior to the measurement, the samples were degassed at 200 °C for 12 h under vacuum. Specific surface areas (S_{BET}) were calculated within the relative pressure range p/p_0 = 0.05−0.2 based on the Brunauer–Emmett–Teller (BET) method. The pore volume (Vp) was determined from the desorption branch of the isotherms at $p/p_0 = 0.95$.

Catalytic CO_2 Hydrogenation

The catalytic performance testing was performed using an in-house built high-pressure setup as presented in the Supporting Information (SI) in Figure S1. 850 mg of the catalyst sieve fraction (200–400 μm grain size) was loaded into a stainless-steel reactor. Firstly, the surface passivation layer of the Co−Fe catalysts was reduced at 450 °C for 8 h in 200 cm^3 STP min^{-1} H_2 flow at ambient pressure. After the reactor was cooled down to 160 °C, the gas flow was switched to the reactant gas mixture (H_2/CO_2/Ar = 60:30:10, Ar as internal GC standard; 56.7 cm^3 STP min^{-1}; 4000 cm^3 h^{-1} $g_{cat}{}^{-1}$) and pressure was built up to 2.0 MPa controlled by a membrane dome regulator. The reaction was started by increasing the reactor temperature to 180 °C with a 1 °C min^{-1} heating ramp.

The outlet gas was analyzed for CO, CO_2, hydrocarbons and methanol by an online gas chromatograph (GC) Agilent 7890B equipped with two TCD and one flame ionization detector (FID). Typical chromatograms are depicted in Figure S2. The activity and selectivity of the catalysts were evaluated after 54 h time-on-stream to ensure a steady reaction state. Additionally, higher boiling oxygenate products were collected in a high-pressure trap downstream the reactor at 20 °C for 72 h. The concentration of the products was determined by high-performance liquid chromatography (HPLC) with a Shimadzu LC-2030 equipped with a Metacarb column (300×7.5 mm) coupled with a refractive index (RI) detector and operated at 50 °C. The mobile phase was 0.1% trifluoroacetic acid (TFA) and a flow rate of 0.8 cm^3 min^{-1} was applied. For additional qualitative analysis of the liquid phase products, nuclear magnetic resonance (^{1}H NMR) spectra were acquired on a Bruker Avance III spectrometer operated at 600 MHz and equipped with a cryogenically cooled TCI probehead. Water suppression at 4.68 ppm was performed by “excitation sculpting”[42] in combination with a “perfect echo”[43] using the Bruker standard pulse-program “zgesgppe”.

In addition to the reaction temperature of 180 °C, the catalytic performance of the silica-supported Co−Fe catalysts was also compared at 220, 280, and 340 °C. Also, selectivity at different reactant gas space velocities of 2000, 4000, 6000, 8000, and 10000 $cm^3\ h^{-1}\ g_{cat}{}^{-1}$ was compared at 180 °C.

2 Results

Catalyst Synthesis and Characterization

Native Co, Fe, and Co−Fe alloy minerals, such as wairauite (CoFe), occur at some silica-rich serpentinizing hydrothermal vents and the same metals also show biocatalytic activity in enzymatic CO_2 fixation. Based on these observations, silica-supported Co−Fe catalysts with varying Co/Fe ratios were synthesized and used for CO_2 hydrogenation toward metabolic intermediates.

The XRD patterns of the calcined monometallic silica-supported Co and Fe catalysts in Figure S3 display the characteristic reflections of the Co_3O_4 spinel phase and the Fe_2O_3 maghemite phase, respectively. For all bimetallic Co−Fe catalysts, only reflections indicative of the spinel structure with space group *Fd-3 m* are observed, which can be attributed to Co_3O_4, Fe_3O_4, and mixed spinel phases, such as $CoFe_2O_4$. As highlighted for the main reflection at 36.9° 2θ indexed to the (311) plane, the reflections of the bimetallic materials are shifted toward lower angles with increasing Fe content. The increase in the lattice parameter results from the slightly larger ionic radius of Fe^{3+} (0.645 Å) compared to Co^{3+} (0.610 Å).[44] A reflection broadening for the bimetallic Co−Fe catalysts hints at smaller crystallite sizes compared to the monometallic counter-parts and a decreasing crystallite size with increasing Fe content. Slight asymmetries in the reflection shapes indicate the formation of crystallites with varying Co/Fe ratios.

At serpentinizing hydrothermal systems, the transition metal-containing minerals can be reduced to the zero-valent metallic phase by the abundant H_2 supply. Thus, the reducibility of the silica-supported metal oxide nanoparticles with varying Co/Fe ratios was investigated by the analytical method of H_2-TPR. The details of the measurement procedure for this chemisorption method are described in the experimental section. As shown in Figure 1a, two signals centered at ~280 and ~360 °C are observed for the monometallic Co-based catalyst, which are characteristic of the stepwise reduction of Co_3O_4 to Co^0 via the CoO intermediate.[45] The additional shoulder at ~580 °C can be associated with the reduction of Co species strongly interacting with the silica support, such as $Co{-}O{-}SiO_x$ or cobalt silicate, which was also observed in our previous study on silica-supported Co catalysts.[38] The reduction pattern of the monometallic Fe-based nanoparticles exhibits three signals in the temperature range up to 700 °C. The signals indicate the stepwise reduction of Fe_2O_3 to Fe^0 via Fe_3O_4 and 'FeO' intermediates at ~340, ~450, and ~620 °C, respectively.[46] Overall, the reduction occurs at higher temperatures compared to the Co catalyst and the pronounced signal at $T>900$ °C indicates the additional formation of a substantial amount of hardly reducible Fe species due to a stronger interaction with the silica support. As a result of overlaying signals from the reduction of different Fe and Co species, the H_2-TPR profiles of the bimetallic Co−Fe materials are more complex. However, the highlighted shift of the first reduction signal assigned to the reduction of Co^{3+} to Co^{2+} toward higher temperatures with increasing Fe content shows the tendency of Fe to increase the reduction temperature of Co. On the other hand, the absence of the high-temperature signal ($T>900$ °C) for the bimetallic catalysts indicates enhanced reducibility of the Fe species in the presence of Co.[47,48]

As the dynamic process during the H_2-TPR experiment differs from the static reduction step during the catalyst synthesis, additional reduction profiles of the as-reduced and surface-passivated materials were collected for selected samples (see Figure 1b). All materials show one broad reduction signal at $T < 450$ °C indicative for the reduction of a divalent surface metal oxide layer. Due to the additional reduction signal observed at ~700 °C for the pre-reduced bimetallic catalysts, the H_2 consumption of the metal oxides in the temperature range of 50–700 °C was chosen as an estimate for the comparison of the molar metal amounts after reduction. As summarized in Table S1, the molar metal amount of monometallic Fe supported on silica was lowest (0.95 mmol g_{cat}^{-1}), while Co was most completely reducible (2.04 mmol g_{cat}^{-1}) and the bimetallic Co−Fe catalysts contained similar, intermediate amounts of metal species (1.67–1.89 mmol g_{cat}^{-1}). The amount of reducible transition metal species is important for the discussion of the catalytic activity in CO_2 hydrogenation since the metallic phase is typically considered the active species for CO_2 activation over silica-supported Co-based catalysts.[49,50]

The reduction of the Fe- and Co-based catalysts to the metallic phase after the treatment at 450 °C in H_2 is further confirmed by the XRD patterns, as seen in Figure S4. The monometallic materials show reflections corresponding to the *bcc* α-Fe phase and the *fcc* β-Co phase, respectively. For Co_3Fe_5 and the bimetallic catalysts with higher Co content, the shift in the reflection indexed to the (110) plane toward higher angles compared to the Fe-based catalyst (44.7° 2θ) suggests the formation of the CoFe alloy wairauite. The reflection patterns show crystallite growth during the reduction step especially for the Fe-rich catalysts and signal asymmetry is indicative for crystallites with different Co/Fe ratios. Additional broad signals corresponding to the Fe_3O_4 phase (at 35.4 and 62.5° 2θ) and CoO phase (at 36.5, 42.4, and 61.5° 2θ) can be explained by the oxide passivation layer on the surface of the metal nanoparticles or incomplete reduction during the hydrogen treatment.

The actual metal loadings and metal ratios of the silica-supported catalysts were determined by bulk SEM–EDX analysis. As summarized in Table S2, the molar Co/Fe ratios and total metal loadings (15.5–18.2 wt %) agree well with the predicted values from the catalyst synthesis. The local metal distribution was exemplarily investigated for the CoFe catalyst by HAADF–STEM coupled with EDX and the Co/Fe 1/1 ratio was also confirmed for the area depicted in Figure 2a. In agreement with the XRD data, the Co and Fe elemental mappings in Figure 2b–d indicate a mostly homogeneous distribution of both metals over the silica support with some Co- or Fe-rich particles. As seen from the line scan in Figure 2e, both metals Co and Fe are distributed homogeneously from the surface to the core of the bimetallic nanoparticles. Also, the lattice fringe spacings determined from the HR–TEM micrograph (Figure 2f) correspond to the formation of the CoFe alloy wairauite. The metal particle size distributions determined from TEM micrographs show overall similar mean particle diameters of 7.2–12.4 nm for all catalysts (see Figure S5a–g). However, the particle sizes of the bimetallic catalysts are slightly decreased compared to the monometallic counterparts, especially in the case of the Fe-rich alloys.

The textural properties of the catalysts were further compared by N_2 physisorption analysis. All materials possess type-IV isotherms with an H1 hysteresis loop characteristic for the mesoporous silica support (see Figure S6). The specific surface areas (258–285 $m^2\ g^{-1}$) and pore volumes (0.89–0.99 $cm^3\ g^{-1}$) of all catalysts were similar and slightly decreased compared to the pristine silica support (see Table S2).

Prebiotic Carbon Compounds in the Liquid Phase

Our previous studies demonstrated catalytic activity of nanostructured Fe−Ni alloy catalysts for CO_2 fixation to formate, acetate, ethanol, and pyruvate at temperatures of 60–100 °C and a pressure of 2.5 MPa under hydrothermal conditions with and without the addition of molecular H_2.[32,33] He et al. found that physical mixtures of Co and Fe yielded formate and long-chain hydrocarbons as the main products from sodium bicarbonate under simulated hydrothermal vent conditions.[39] Monometallic Co catalysts on different silica-based support materials catalyzed CO_2 reduction to formate, acetate, methanol, and ethanol at realistic hydrothermal vent conditions of 180 °C and 2.0 MPa.[38] Cobalt-iron alloys are naturally deposited as the mineral wairauite in the highly reducing conditions of serpentinizing hydrothermal vents.[51] The effect of alloying Co with Fe has not been investigated in laboratory CO_2 fixation.

Using the same temperatures and pressures previously studied for Co,[38] we investigated silica-supported Co−Fe catalysts for H_2-dependent CO_2 hydrogenation. In addition to the alloyed bimetallic Co−Fe catalysts, a physical mixture of the monometallic Co- and Fe-based catalysts (with an atomic ratio of 1/1) was tested for CO_2 hydrogenation, which is denoted as Co+Fe in the following. Products were analyzed in the gas phase by online GC and in the liquid phase condensed in a cold trap at 20 °C. Quantitative and qualitative analysis of the higher boiling point products in the condensed phase was performed offline by HPLC and ^1H NMR, respectively.

Liquid phase products analyzed by HPLC revealed similarities between CO_2 fixation products obtained over Co−Fe alloys with intermediates in microbial metabolism and products of geochemical CO_2 reduction at serpentinizing hydrothermal vents. The monometallic Fe catalyst and the Fe-rich bimetallic catalysts $CoFe_3$ and Co_3Fe_5 yielded too little condensed phase (< 100 µL) for proper product analysis.

As shown in Figure 3, all of the other catalysts formed formate, acetate, and ethanol from CO_2 reduction in the mM range as detected by HPLC analysis and qualitatively confirmed by ^1H NMR analysis for the Co catalyst, exemplarily (see Figure S7). Methanol was detected in the liquid product phase as well, but was better quantified in the gas phase, as discussed below together with the other gaseous products. The highest concentration of acetate (0.8 mM) was obtained for the CoFe catalyst while all other catalysts yielded a concentration of 0.2 mM. The formation of formate was favored with the 1/1 ratio alloy CoFe (6.0 mM) and tended to decrease with increasing Co content up to 0.7 mM for the monometallic Co catalyst. Ethanol concentration was highest for the CoFe catalyst (8.2 mM) among the bimetallic catalysts and decreased with increasing Co content. However, the monometallic Co catalyst yielded the highest concentration of ethanol (13.7 mM). Overall, the results indicate a synergistic bimetallic effect of the Co−Fe catalysts for formate and acetate formation compared to the monometallic materials. The alloyed CoFe catalyst yields higher formate and acetate selectivities compared to the physical mixture of the monometallic catalysts (Co+Fe) with the same metal ratio. The Co±Fe and monometallic Co catalysts favored ethanol formation. Combining Fe and Co in alloyed active sites enhanced CO_2 hydrogenation to metabolic oxygenates and increased selectivity toward the oxygen-containing products. Alloying with Fe increases the electron density of Co,[52] generating electronic structural changes that can affect the activation energies for different competing reaction pathways (discussed below).

The formation of formate at far higher concentrations compared to acetate (Figure 3) is in line with observations from the effluents of serpentinizing systems. At the Lost City hydrothermal field, abiotic acetate is below detection, while abiotic formate reaches concentrations of 36–158 μM,[12,53] where it serves both as a carbon source for microbial growth and as the second-most abundant reductant after H_2.[53–55] In the acetyl-CoA pathway of CO_2 fixation in acetogens and methanogens,[20] formate is generated as the first intermediate, whereby the methanogen enzyme complex is extremely Fe-rich, containing 46 FeS clusters.[56] Acetyl formation in the pathway requires a cobalt-dependent methyl transfer reaction catalyzed by the cobalamin-containing corrinoid FeS protein, CoFeS.[6,20,37] The acetyl-CoA pathway requires both Co and Fe,[22] but not in alloyed form.

Prebiotic Carbon Compounds in the Gas Phase

Online GC analysis of the gaseous products yields a more complete picture of the bimetallic effects on CO_2 hydrogenation. Catalytic activity and product selectivity were compared after 54 h time-on-stream as the selectivity was found to be stable afterward (see Figure S8a–h). As seen in Figure 4a, the CO_2 reduction activity of the monometallic Fe catalyst was lowest (0.4 %), similar to the Co_3Fe_5 catalyst (0.6%) and then increased mostly linearly with increasing Co content in the bimetallic Co−Fe catalysts (1.4–2.5 %). XRD patterns showed that the bimetallic catalysts all contained a CoFe alloy phase (see Figure S4), indicating a promotional catalytic effect of Co−Fe alloying compared to monometallic Fe. The Co catalyst was clearly the most active (6.3 %). The higher CO_2 conversion with the 1/1 Co+Fe physical mixture compared to the alloys reflects the higher activity of monometallic Co.

The known intrinsic catalytic properties of Fe- and Co-based materials explain the difference in product gas selectivity observed in this study. In Co-based catalysts, typically the metallic phase is considered the main active site for CO_2 adsorption and activation, especially with SiO_2-based supports.[49,50,57] Here, the highest catalytic activity of the monometallic Co catalyst could be correlated with its highest amount of metallic phase among the Co−Fe catalysts according to the H_2-TPR results (see Figure 1 and Table S2). For Fe-based catalysts, however, the situation is more complex. In the literature, several active sites have been discussed for CO_2 hydrogenation over Fe-containing catalysts including metallic iron, iron carbides, and iron oxides (e. g. Fe_3O_4).[58,59] In addition, the reaction mechanism of CO_2 hydrogenation on Fe-based catalysts differs from Co-based catalysts. Fe species are highly active in CO_2 hydrogenation to CO via the endothermic RWGS. In contrast, Co-based catalysts have a high hydrogenation ability and favor CO_2 reduction toward CH_4 via the exothermic Sabatier reaction, which is thermodynamically favorable at the investigated moderate reaction temperatures.[25,60]

The 1/1 ratio CoFe alloy and Co-rich catalysts with the higher hydrogenation activity formed CH_4 as the main product at 48–81% selectivity shown in Figure 4b, whereby the selectivity increased with increasing Co content. In contrast, the Fe-rich catalysts only yielded 7–9% of CH_4 but the selectivity toward CO was enhanced (37–40 %). However, as the main product methanol was obtained with 49–55% selectivity. With increasing Co/Fe ratio, the selectivity toward methanol was decreased and the monometallic Co catalyst produced only 11% methanol. Instead, the Co-rich catalysts favored C−C bond coupling and produced linear hydrocarbons up to *n*-heptane, while only C_2 and C_3 products were obtained with the Fe-rich materials. Previous studies on Co−Fe catalysts reported a synergistic promotion effect for C_{2+} hydrocarbon formation via FTS.[25,48] Here, Co_5Fe_3 gave the highest hydrocarbon selectivity. The selectivities of the 1/1 CoFe catalyst and Co-richer catalysts were comparable (see Figure 4b).

The formation of CH_4 and low-molecular weight hydrocarbons underscores the similarity between reactions on catalysts in this study and CO_2 reduction catalyzed by minerals at hydrothermal vents. In the effluent of serpentinizing systems, high concentrations of abiotically formed CH_4 and low molecular-weight hydrocarbons have been observed.[10,11] While other experimental studies simulating CO_2 fixation under hydrothermal vent conditions mostly reported the synthesis of $C_{<5}$ hydrocarbons, we were able to obtain a mixture of CO_2 reduction products.[61] It should be emphasized that the abiotic synthesis of methane and short chain hydrocarbons in serpentinizing systems is not simple to ascertain nor is it undebated; a number of factors figure into the issue, and the criteria for abiotic synthesis can vary across geological sites, as recently reviewed by Etiope and Oze.[62]

Comparison of Product Formation via Formate and CO routes

Figure 5 summarizes the catalyst comparison. The results suggest a lower activity of the Fe-rich catalysts for C–O bond cleavage by hydrogenation with the favored formation of the oxygen-containing products CO and methanol, whereas the Co-rich catalysts tended to form the more hydrogenated products, CH_4 and higher hydrocarbons. The characteristic shift in the product selectivites was most pronounced from the Co_3Fe_5 catalyst to the 1/1 ratio CoFe catalyst. Compared to 1/1 Co+Fe, the alloy yielded a higher selectivity for the oxygenate products and less CH_4, suggesting that alloying suppressed the hydrogenation activity.[60] The overall selectivity of the physical mixture resembled the monometallic Co catalyst, probably due to its dominant activity compared to the Fe counterpart under these conditions.

Comparing the gas phase and the liquid phase results for oxygenate product formation, selectivity for methanol followed a similar trend as the organic acids and decreased in concentration with increasing Co content. However, the concentration of ethanol was highest with the monometallic Co catalyst, as in earlier studies.[63] Mechanistically, methanol can either be formed via a formate intermediate or *CO generated from RWGS.[57,64] Over Co-based catalysts, the reaction is expected to proceed preferentially via the formate intermediate.[57,65] Formate can either be released or hydrogenated further to methanol and CH_4. The promoted formation of both methanol and formate by the combination of Co with Fe, as shown in Figure 5, might result from the suppression of the activity for deep hydrogenation of the formate intermediate by Fe. Over Fe-based catalysts, *CO (instead of formate) is typically generated as the predominant intermediate in CO_2 activation via C−O bond scission. However, the mechanism for the formation of methanol is not well studied as the reaction is thermodynamically unfavorable under the typical high reaction temperatures with Fe-based catalysts, although Fe carbides have been reported to form a substantial amount of methanol at reaction temperatures of 220 °C.[66]

The formation of C_2 oxygenate products from CO_2 requires balanced abilities of the catalyst for both CO_2 and H_2 activation. Mechanistically, ethanol is typically formed from the further hydrogenation of an acetate group.[27] Compared to the C_1 intermediates for methanol synthesis, which can be produced from CO_2 readily after its adsorption and activation, the generation of acetate includes an additional insertion step for C−C bond formation. This C−C coupling step is typically considered a critical step in ethanol formation.[63] Again, two different pathways are possible for acetate formation either via insertion of a $*CH_x$ species bound to the catalyst surface into a *CO intermediate formed by RWGS or a formate intermediate as C_1-oxygen species.[67,68] In either route, $*CH_x$ species are the key species for the C−C bond formation step.[22] Thus, in addition to a sufficient C−C coupling activity of the catalyst, the highest concentration of $*CH_x$ species as intermediates for CH_4 on the monometallic Co catalyst probably promotes coupling with $*C_1$-oxygen species for the formation of C_2-oxygen species.[63,69] The C=O bond in acetate is weakened compared to the formate species and thus further hydrogenation toward the ethoxy group is facilitated.[63] Therefore, the Co catalyst with the high hydrogenation ability probably hydrogenated most of the C_2 oxygenate products further to ethanol (see Figure 5).[28] The CoFe alloy with intermediate C−C coupling and hydrogenation abilities as well as balanced concentrations of $*C_1$-oxygen and $*CH_x$ species on the surface yielded higher concentrations of both organic acids.

Differences in Hydrogen Adsorption

The binding strength of a catalyst with the reactants in the initiation step of adsorption and activation is important for its overall catalytic performance. We performed H_2-TPD experiments to compare the adsorption properties of the Co−Fe catalysts and explain the observed trend in the hydrogenation ability. The H_2 desorption profiles in Figure 6 present a low-temperature signal centered at around 100–200 °C for all catalysts. This signal can be ascribed to H species adsorbed on metallic Fe or Co sites and was thus not observed with the pristine silica support.[70,71] The shift in the temperature of desorption indicates that H_2 adsorption was weakest on the monometallic Co-based catalyst and enhanced with increasing Fe content. As this was the only H_2 desorption signal observed for the Co catalyst with the highest CH_4 selectivity, weak H_2 adsorption appeared favorable for CO_2 hydrogenation toward CH_4 via the formate pathway.

All Fe-containing catalysts exhibited additional high-temperature H_2 desorption signals at 500–800 °C. These signals were steadily enhanced with increasing Fe content. In agreement with the EDX line scan data, this indicates a homogeneous distribution of Fe and Co throughout the bimetallic nanoparticles and no surface aggregation of one metal species. Similar high-temperature H_2-TPD signals of Fe-based catalysts have been reported, the strong H_2 adsorption was related to the presence of difficult to reduce iron oxides or silicates.[70,71] The preferentially strong adsorption of hydrogen might suppress the adsorption and activation of CO_2, which could help to account for the lower catalytic activity of the Fe-containing catalysts.[72,73] Also, a high H/C ratio on the catalyst surface decreases chain growth probability as observed in only C_3 hydrocarbon formation with the Fe-rich catalysts while Co-rich catalysts yielded hydrocarbons up to C_7, as depicted in Figure 5. Yet the hydrogenation of surface carbon species to CH_4 can also be restrained by a higher activation energy for the strongly adsorbed hydrogen.[74] As a consequence, methanol and CO were preferentially formed with Fe-rich catalysts as opposed to sequential hydrogenation of reaction intermediates toward CH_4.

Kinetic Indications of Gas Phase Product Selectivity

For further kinetic investigations, the effect of the variation of the reactant gas space velocity, defined as volume flow per hour and mass of catalyst, on the product selectivity in the gas phase was also studied. By varying the contact time between catalyst and reactant gas, reaction rates for the formation of the different products can be compared and reaction pathways can be contrasted. As seen in Figure 7a–c and Figure S9a–e, clear differences in the behavior of the Fe- and Co-rich catalysts are observed. The selectivity toward the gas phase products appeared to be largely independent of the space velocity for all Fe-rich catalysts. The selectivity toward CH_4 was only slightly enhanced relative to CO at longer contact times.

Typically, the formation of CH_x species over Fe-based catalysts is assumed to occur via the hydrogenation of the *CO intermediate.[75] However, the overall hydrogenation ability of the catalysts appeared low even at slow gas flows. In contrast, on the Co-based catalyst the selectivity toward the hydrogenated products, CH_4 and C_{2+} hydrocarbons, clearly decreased relative to methanol with shorter residence times at increasing gas space velocity (see Figure 7c). In case of the monometallic Co catalyst, the deep hydrogenation of CO_2 to CH_4 requiring C−O bond scission appeared slower compared to methanol formation.[64] Lower space velocities not only promoted the hydrogenation toward CH_4, but also favored the C−C coupling of the CH_x surface species to hydrocarbons. The CO formation was not competitive and its selectivity was low at all space velocities.

For the alloyed CoFe catalyst, the selectivity toward CO and methanol increased in parallel with the decrease in CH_4 and C_{2+} hydrocarbon selectivity at shorter residence times (see Figure 7b). The complete hydrogenation of CO_2 competed with the formation of both oxygenate products. This indicated interconnected pathways for the formation of all four products. The reaction might proceed via the two different pathways characteristic of the Co and Fe active sites: the formate and CO-mediated pathway. A higher overall hydrogenation ability in the presence of Co species might promote the hydrogenation of the *CO intermediate to CH_4 over the Fe active sites at longer contact times.

In agreement with a two-step mechanism for CO_2 hydrogenation to hydrocarbons via a CO intermediate over Fe-based catalysts, an increase in CO selectivity at shorter residence times was observed while hydrocarbon selectivity increased at longer residence times.[76] At the more moderate reaction temperature in this study, strong H_2 adsorption (see Figure 6) and high activation energies for C−O bond cleavage possibly slowed down CH_4 formation on the Fe-rich catalysts irrespective of the gas space velocity.[60] Thus, the oxygenate product selectivity only showed a slight dependence on the residence time for the monometallic Fe catalyst while the effect was more pronounced with the CoFe catalyst.

Effects of Reaction Temperature

To investigate the effect of the reaction temperature on catalyst performance, the catalytic activity and gas phase product selectivities at 180, 220, 280, and 340 °C were compared to cover the upper temperature range that might be expected at serpentinizing systems.[9,13] As seen in Figure 8, the catalytic activity was enhanced with increasing reaction temperature for all materials, but the monometallic Co catalyst remained clearly the most active with 35% CO_2 conversion at the highest temperature. The other catalysts yielded 10–22% conversion at 340 °C. Also, a strong influence of the reaction temperature on the product selectivities of all catalysts was revealed. In general, higher temperatures promoted CO_2 methanation relative to desorption of oxygenate intermediates (see Figure 8b). Although being exothermic in nature and thermodynamically favorable at lower temperatures, the reaction can be kinetically hindered at lower temperatures.[77] At all temperatures, the CH_4 selectivity of the Fe-rich catalysts was significantly lower compared to the CoFe and Co-rich catalysts with higher hydrogenation ability. For the alloyed Co-rich catalysts, the selectivity toward CH_4 went through a maximum of 79–88% at 280 °C, while it increased up to 340 °C with 32–37% selectivity for the Fe-rich catalysts. The monometallic Co catalyst yielded the highest CH_4 selectivity of 94% at 340 °C.

The endothermic RWGS for CO formation becomes more favorable at higher temperatures and overall increases with increasing reaction temperature as shown in Figure 8c. The Fe-rich catalysts yielded the highest selectivities of 56–58% CO, in contrast to CH_4 selectivties, while CoFe and the Co-rich catalysts only reached 5–21 %. Regarding the selectivity toward C_{2+} hydrocarbons, the trend of the Co−Fe catalysts was inconsistent, although the selectivity was clearly highest at 340 °C with the monometallic Fe catalyst (11 %), while the bimetallic catalysts yielded 5–8% and the Co catalyst only 2% (see Figure S10). The more moderate hydrogenation ability probably favored C−C coupling over the desorption of CH_x intermediates as CH_4 over the Fe catalyst.

As shown in Figure 8d, methanol formation had the strongest temperature dependence for all catalysts. The exothermic methanol synthesis reaction was favored at lower temperatures and its selectivity was already decreased by more than half at 220 °C compared to 180 °C for the Co-rich catalysts. The methanol selectivity was further diminished to 1% for all catalysts at 340 °C. Thus, for partial CO_2 hydrogenation to oxygenate products relative to CH_4 formation, the lower, more biocompatible temperature range was more favorable.[6]

3 Conclusions

Among the silica-supported Co−Fe catalysts investigated here, the 1/1 CoFe alloy with the same composition as the natural mineral wairauite yielded the highest concentrations of the intermediate metabolic products acetate (0.8 mM) and formate (6.0 mM) from CO_2

reduction. As in the effluent of hydrothermal vents, additional CH_4 and low-molecular weight hydrocarbons were obtained together with methanol, ethanol, and CO. Generally, the Co-rich catalysts favored CO_2 methanation and the formation of hydrocarbons, while the Fe-rich catalysts formed methanol and CO as the main products. The results reveal a striking similarity between the role of the Co active site in natural mineral catalysts and in the corrinoid iron sulfur (CoFeS) enzyme of methyl transfer in the acetyl-CoA pathway, the most ancient pathway of biological CO_2 fixation, further narrowing the gaps between mineral catalyzed and enzymatic CO_2 reduction. The alloying of both metals suppressed hydrogenation activity compared to the physical mixture. Mechanistically, the formation of CH_4 and oxygenate products from the same intermediates over the CoFe catalyst is suggested, with a slower reaction rate for full hydrogenation. Across a temperature range simulating hydrothermal vent conditions, the formation of oxygenate products typical of metabolism was clearly favored at the lower, more biocompatible temperature range. Overall, our study demonstrates similarities between H_2-dependent CO_2 reduction by Co−Fe catalysts in natural minerals and their biological derivatives as Co and Fe cofactors in the acetyl-CoA pathway of H_2-dependent autotrophic anaerobes.

Supplementary Material

Refer to Web version on PubMed Central for supplementary material.

Acknowledgements

This work was funded by the Volkswagen Foundation (96_742) and Deutsche Forschungsgemeinschaft (MA-1426/21-1/TU 315/8-1). H.T. thanks the Max Planck Society and the FUNCAT Centre, W.M thanks the ERC (101018894) for funding. We thank Dr. Tuğçe Beyazay and Dr. Youngdong Song for the fruitful discussion. Further, we acknowledge Dr. Eko Budiyanto and Silvia Palm for microscopy images and EDX analyses, and Jan Ternieden for XRD measurements. Heike Hinrichs is thanked for HPLC analysis and Dr. Christophe Farès for NMR analysis. Open Access funding enabled and organized by Projekt DEAL.

Data Availability Statement

The data that support the findings of this study are available from the corresponding author upon reasonable request.

References

[1]. Oparin, AI. The origin of life. The MacMillan Company; New York City: 1938. 127

[2]. Haldane JBS. Rationalist Annual. 1929; 148: 3–10.

[3]. Chyba C. Nature. 1992; 355: 125–132. [PubMed: 11538392]

[4]. Cooper G, Kimmich N, Belisle W, Sarinana J, Brabham K, Garrel L. Nature. 2001; 414: 879–883. DOI: 10.1038/414879a [PubMed: 11780054]

[5]. Engel MH, Macko SA, Silfer JA. Nature. 1990; 348: 47–49. DOI: 10.1038/348047a0 [PubMed: 11536470]

[6]. Martin W, Russell MJ. Philos Trans R Soc B. 2007; 362: 1887–1926. DOI: 10.1098/rstb.2006.1881

[7]. Martin W, Baross J, Kelley D, Russell MJ. Nat Rev Microbiol. 2008; 6: 805–814. DOI: 10.1038/nrmicro1991 [PubMed: 18820700]

[8]. Kelley DS, Karson JA, Blackman DK, Früh-Green GL, Butter-field DA, Lilley MD, Olson EJ, Schrenk MO, Roe KK, Lebon GT. Nature. 2001; 412: 145–149. DOI: 10.1038/35084000 [PubMed: 11449263]

[9]. Kelley DS, Baross JA, Delaney JR. Annu Rev Earth Planet Sci. 2002; 30: 385–491. DOI: 10.1146/annurev.earth.30.091201.141331

[10]. Kelley DS, Karson JA, Früh-Green GL, Yoerger DR, Shank TM, Butterfield DA, Hayes JM, Schrenk MO, Olson EJ, Proskurowski G, Jakuba M, et al. Science. 2005; 307: 1428–1434. DOI: 10.1126/science.1102556 [PubMed: 15746419]

[11]. Proskurowski G, Lilley MD, Seewald JS, Früh-Green GL, Olson EJ, Lupton JE, Sylva SP, Kelley DS. Science. 2008; 319: 604–607. [PubMed: 18239121]

[12]. Lang SQ, Butterfield DA, Schulte M, Kelley DS, Lilley MD. Geochim Cosmochim Acta. 2010; 74: 941–952. DOI: 10.1016/j.gca.2009.10.045

[13]. Humphris SE, Klein F. Ann Rev Mar Sci. 2018; 10: 315–343. [PubMed: 28853997]

[14]. Klein F, Bach W. J Petrol. 2009; 50: 37–59. DOI: 10.1093/petrology/egn071

[15]. Charlou JL, Donval JP, Fouquet Y. Chem Geol. 2002; 191: 345–359. DOI: 10.1016/S0009-2541(02)00134-1

[16]. Klein F, Bach W, Jöns N, McCollom T, Moskowitz B, Berquó T. Geochim Cosmochim Acta. 2009; 73: 6868–6893. DOI: 10.1016/j.gca.2009.08.021

[17]. Evans BW, Hattori K, Baronnet A. Elements. 2013; 9: 99–106. DOI: 10.2113/gselements.9.2.99

[18]. Russell MJ, Martin W. Trends Biochem Sci. 2004; 29: 358–363. DOI: 10.1016/j.tibs.2004.05.007 [PubMed: 15236743]

[19]. Ragsdale SW, Pierce E. Biochim Biophys Acta. 2008; 1784: 1873–1898. DOI: 10.1016/j.bbapap.2008.08.012 [PubMed: 18801467]

[20]. Fuchs G. Annu Rev Microbiol. 2011; 65: 631–658. [PubMed: 21740227]

[21]. Berg IA, Kockelkorn D, Ramos-Vera WH, Say RF, Zarzycki J, Hügler M, Alber BE, Fuchs G. Nat Rev Microbiol. 2010; 8: 447–460. DOI: 10.1038/nrmicro2365 [PubMed: 20453874]

[22]. Gao P, Zhang L, Li S, Zhou Z, Sun Y. ACS Cent Sci. 2020; 6: 1657–1670. DOI: 10.1021/acscentsci.0c00976 [PubMed: 33145406]

[23]. Wang Y, Winter LR, Chen JG, Yan B. Green Chem. 2021; 23: 249–267. DOI: 10.1039/D0GC03506H

[24]. Goud D, Gupta R, Maligal-Ganesh R, Peter SC. ACS Catal. 2020; 10: 14258–14282. DOI: 10.1021/acscatal.0c03799

[25]. Satthawong R, Koizumi N, Song C, Prasassarakich P. Top Catal. 2014; 57: 588–594. DOI: 10.1007/s11244-013-0215-y

[26]. Gnanamani MK, Jacobs G, Hamdeh HH, Shafer WD, Liu F, Hopps SD, Thomas GA, Davis BH. ACS Catal. 2016; 6: 913–927. DOI: 10.1021/acscatal.5b01346

[27]. Xu D, Wang Y, Ding M, Hong X, Liu G, Tsang SCE. Chem. 2021; 7: 849–881. DOI: 10.1016/j.chempr.2020.10.019

[28]. Gnanamani MK, Hamdeh HH, Jacobs G, Shafer WD, Hopps SD, Thomas GA, Davis BH. ChemCatChem. 2017; 9: 1303–1312. DOI: 10.1002/cctc.201601337

[29]. Takahashi H, Liu LH, Yashiro Y, Ioku K, Bignall G, Yamasaki N, Kori T. J Mater Sci. 2006; 41: 1585–1589. DOI: 10.1007/s10853-006-4649-5

[30]. He C, Tian G, Liu Z, Feng S. Org Lett. 2010; 12: 649–651. DOI: 10.1021/ol9025414 [PubMed: 20104858]

[31]. Varma SJ, Muchowska KB, Chatelain P, Moran J. Nat Ecol Evol. 2018; 2: 1019–1024. DOI: 10.1038/s41559-018-0542-2 [PubMed: 29686234]

[32]. Preiner M, Igarashi K, Muchowska KB, Yu M, Varma SJ, Kleinermanns K, Nobu MK, Kamagata Y, Tüysüz H, Moran J, Martin WF. Nat Ecol Evol. 2020; 4: 534–542. DOI: 10.1038/s41559-020-1125-6 [PubMed: 32123322]

[33]. Beyazay T, Ochoa-Hernández C, Song Y, Belthle KS, Martin WF, Tüysüz H. Angew Chem Int Ed. 2023; 62 e202218189

[34]. Beyazay T, Belthle KS, Farès C, Preiner M, Moran J, Martin WF, Tüysüz H. Nat Commun. 2023; 14: 570. doi: 10.1038/s41467-023-36088-w [PubMed: 36732515]

[35]. Muchowska KB, Varma SJ, Moran J. Chem Rev. 2020; 120: 7708–7744. [PubMed: 32687326]

[36]. Roldan A, Hollingsworth N, Roffey A, Islam H-U, Goodall JBM, Catlow CRA, Darr JA, Bras W, Sankar G, Holt KB, Hogarth G, et al. Chem Commun. 2015; 51: 7501–7504. DOI: 10.1039/C5CC02078F

[37]. Svetlitchnaia T, Svetlitchnyi V, Meyer O, Dobbek H. Proc Natl Acad Sci USA. 2006; 103: 14331–14336. [PubMed: 16983091]

[38]. Belthle KS, Beyazay T, Ochoa-Hernández C, Miyazaki R, Foppa L, Martin WF, Tüysüz H. J Am Chem Soc. 2022; 144: 21232–21243. DOI: 10.1021/jacs.2c08845 [PubMed: 36350298]

[39]. He D, Wang X, Yang Y, He R, Zhong H, Wang Y, Han B, Jin F. Proc Natl Acad Sci USA. 2021; 118 e2115059118 [PubMed: 34911765]

[40]. Peters S, Semenov DA, Hochleitner R, Trapp O. Sci Rep. 2023; 13: 6843. [PubMed: 37231067]

[41]. Frost BR, Beard JS. J Petrol. 2007; 48: 1351–1368. DOI: 10.1093/petrology/egm021

[42]. Hwang TL, Shaka AJ. J Magn Reson Ser A. 1995; 112 (2) 275–279.

[43]. Adams RW, Holroyd CM, Aguilar JA, Nilsson M, Morris GA. Chem Commun. 2013; 49: 358–360. DOI: 10.1039/C2CC37579F

[44]. Shannon RD. Acta Crystallogr Sect A. 1976; 32: 751–767. DOI: 10.1107/S0567739476001551

[45]. Borg Ø, Rønning M, Storsæter S, Holmen A. Stud Surf Sci Catal. 2007; 163: 255–272.

[46]. Brown R, Cooper ME, Whan DA. Appl Catal. 1982; 3: 177–186. DOI: 10.1016/0166-9834(82)80090-0

[47]. Duvenhage DJ, Coville NJ. Appl Catal A. 1997; 153: 43–67. DOI: 10.1016/S0926-860X(96)00326-2

[48]. Griboval-Constant A, Butel A, Ordomsky VV, Chernavskii PA. Appl Catal A. 2014; 481: 116–126. DOI: 10.1016/j.apcata.2014.04.047

[49]. Melaet G, Ralston WT, Li CS, Alayoglu S, An K. J Am Chem Soc. 2014; 136: 2260–2263. DOI: 10.1021/ja412447q [PubMed: 24460136]

[50]. ten Have IC, Kromwijk JJG, Monai M, Ferri D, Sterk EB, Meirer F, Weckhuysen BM. Nat Commun. 2022; 13: 324. doi: 10.1038/s41467-022-27981-x [PubMed: 35031615]

[51]. Chamberlain JA, McLeod CR, Traill RJ, Lachance GR. Can J Earth Sci. 1965; 2 (3) 188–215.

[52]. Lv Y, Han M, Gong W, Wang D, Chen C, Wang G, Zhang H, Zhao H. Angew Chem Int Ed. 2020; 59: 23521–23526. DOI: 10.1002/anie.202009913

[53]. Lang SQ, Früh-Green GL, Bernasconi SM, Brazelton WJ, Schrenk MO, McGonigle JM. Sci Rep. 2018; 8: 755. [PubMed: 29335466]

[54]. Brazelton WJ, McGonigle JM, Motamedi S, Pendleton HL, Twing KI, Miller BC, Lowe WJ, Hoffman AM, Prator CA, Chadwick GL. Appl Environ Microbiol. 2022; 88 e00929-e00922 [PubMed: 35950875]

[55]. Fones EM, Colman DR, Kraus EA, Stepanauskas R, Templeton AS, Spear JR, Boyd ES. ISME J. 2021; 15: 1121–1135. DOI: 10.1038/s41396-020-00838-1 [PubMed: 33257813]

[56]. Wagner T, Ermler U, Shima S. Science. 2016; 354: 114–117. DOI: 10.1126/science.aaf9284 [PubMed: 27846502]

[57]. Fan T, Liu H, Shao S, Gong Y, Li G, Tang Z. J Phys Chem Lett. 2021. 10486–10496. [PubMed: 34677985]

[58]. Riedel T, Schulz H, Schaub G, Jun K-W, Hwang J-S, Lee K-W. Top Catal. 2003; 26: 41–54.

[59]. Puga AV. Catal Sci Technol. 2018; 8: 5681–5707. DOI: 10.1039/C8CY01216D

[60]. Calizzi M, Mutschler R, Patelli N, Migliori A, Zhao K, Pasquini L, Zuttel A. Nanomaterials. 2020; 10: 1360. doi: 10.3390/nano10071360 [PubMed: 32664610]

[61]. Glasby GP. Resour Geol. 2006; 56: 83–96. DOI: 10.1111/j.1751-3928.2006.tb00271.x

[62]. Etiope G, Oze C. Appl Geochem. 2022; 143 105373

[63]. Wang L, Wang L, Zhang J, Liu X, Wang H, Zhang W, Yang Q, Ma J, Dong X, Yoo SJ, Kim JG, et al. Angew Chem Int Ed. 2018; 57: 6104–6108. DOI: 10.1016/j.apgeochem.2022.105373

[64]. Kattel S, Liu P, Chen JG. J Am Chem Soc. 2017; 139: 9739–9754. DOI: 10.1021/jacs.7b05362 [PubMed: 28650651]

[65]. Li K, Li X, Li L, Chang X, Wu S, Yang C, Song X, Zhao ZJ, Gong J. JACS Au. 2023; 3: 508–515. DOI: 10.1021/jacsau.2c00632 [PubMed: 36873681]

[66]. Dubois JL, Sayama K, Arakawa H. Chem Lett. 1992; 21: 5–8. DOI: 10.1246/cl.1992.5

[67]. Bai S, Shao Q, Wang P, Dai Q, Wang X, Huang X. J Am Chem Soc. 2017; 139: 6827–6830. DOI: 10.1021/jacs.7b03101 [PubMed: 28485583]

[68]. Ye R-P, Ding J, Gong W, Argyle MD, Zhong Q, Wang Y, Russell CK, Xu Z, Russell AG, Li Q, Fan M, et al. Nat Commun. 2019; 10: 5698. doi: 10.1038/s41467-019-13638-9 [PubMed: 31836709]

[69]. Wang L, He S, Wang L, Lei Y, Meng X, Xiao F-S. ACS Catal. 2019; 9: 11335–11340. DOI: 10.1021/acscatal.9b04187

[70]. Satthawong R, Koizumi N, Song C, Prasassarakich P. Catal Today. 2015; 251: 34–40. DOI: 10.1016/j.cattod.2015.01.011

[71]. Suo H, Wang S, Zhang C, Xu J, Wu B, Yang Y, Xiang H, Li Y-W. J Catal. 2012; 286: 111–123. DOI: 10.1016/j.jcat.2011.10.024

[72]. Wang H, Nie X, Chen Y, Guo X, Song C. J CO2 Util. 2018; 26: 160–170. DOI: 10.1016/j.jcou.2018.05.003

[73]. Wang H, Nie X, Guo X, Song C. J CO2 Util. 2016; 15: 107–114. DOI: 10.1016/j.jcou.2016.02.010

[74]. Numpilai T, Chanlek N, Poo-Arporn Y, Cheng CK, Siri-Nguan N, Sornchamni T, Chareonpanich M, Kongkachuichay P, Yigit N, Rupprechter G, Limtrakul J, et al. ChemCatChem. 2020; 12: 3306–3320. DOI: 10.1002/cctc.202000347

[75]. Nie X, Wang H, Janik MJ, Chen Y, Guo X, Song C. J Phys Chem C. 2017; 121: 13164–13174. DOI: 10.1021/acs.jpcc.7b02228

[76]. Riedel T, Schaub G, Jun K-W, Lee K-W. Ind Eng Chem Res. 2001; 40: 1355–1363. DOI: 10.1021/ie000084k

[77]. Liu H, Xu S, Zhou G, Xiong K, Jiao Z, Wang S. Fuel. 2018; 217: 570–576. DOI: 10.1016/j.fuel.2017.12.112

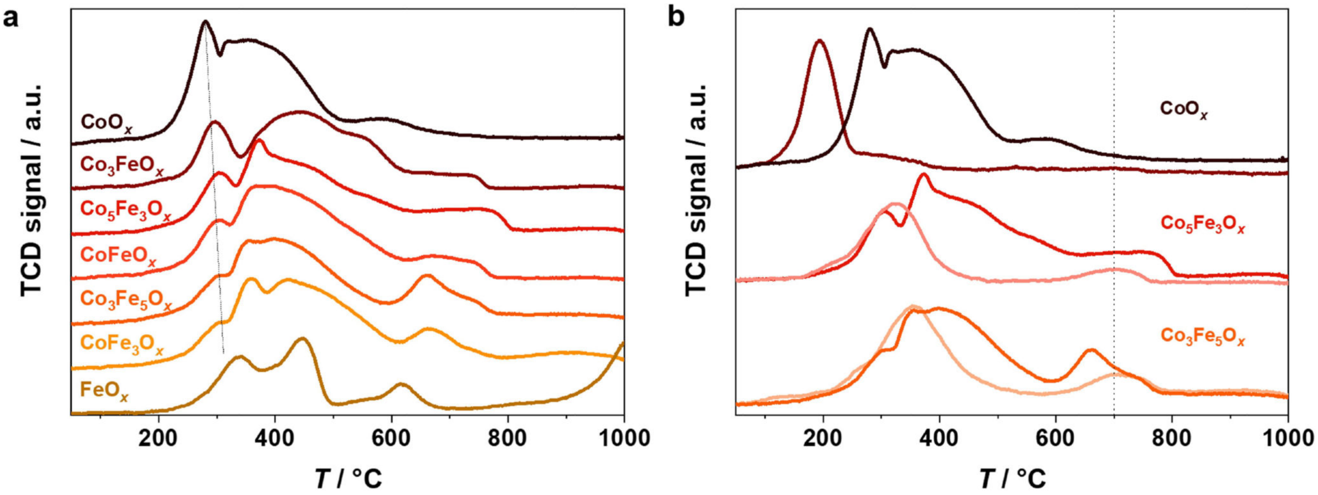

Figure 1.

(a) H_2-TPR profiles of calcined Co−Fe catalysts. (b) Comparison of H_2-TPR profiles of selected Co−Fe catalysts after calcination (dark color) and after reduction with H_2 at 450 °C with subsequent surface passivation (light color).

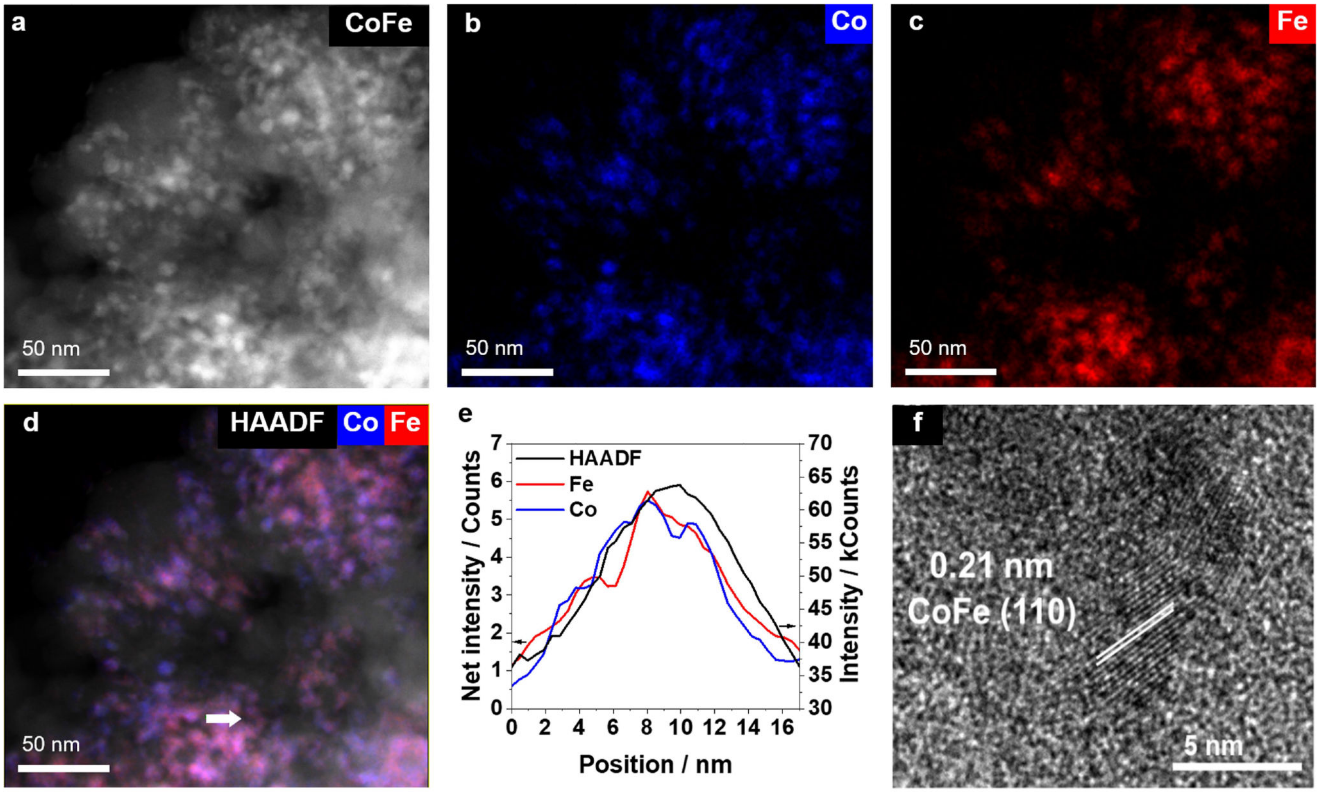

Figure 2.

(a) HAADF image, (b) Co and (c) Fe EDX elemental mappings, (d) combined Fe and Co elemental mappings (arrow indicates the region for the EDX line scan), (e) EDX line scan, and (f) HR–TEM micrograph of the silica-supported CoFe catalyst.

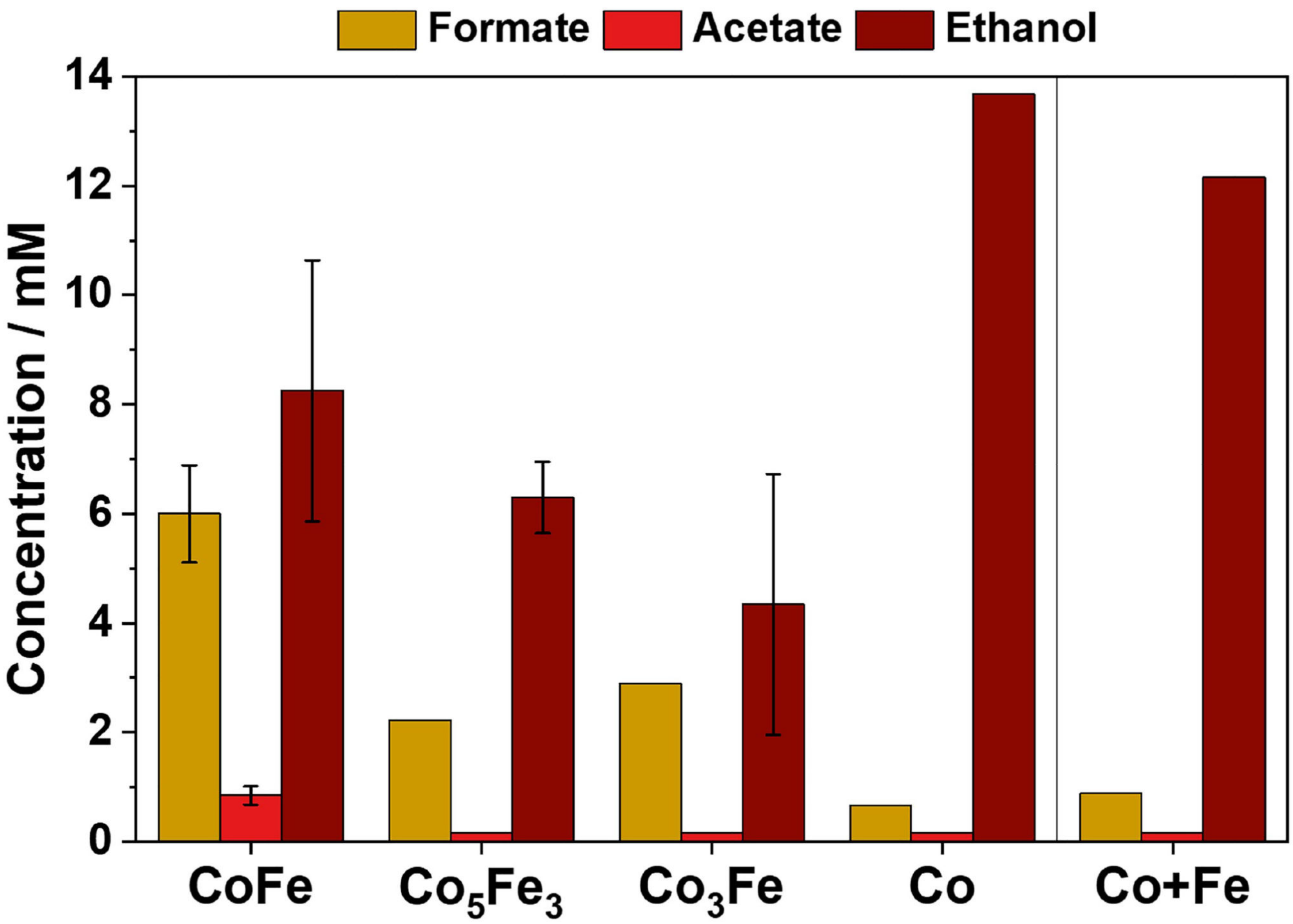

Figure 3.

Concentrations of oxygenate products from CO_2 hydrogenation with silica-supported Co−Fe catalysts determined by HPLC for the liquid product phase collected after 72 h time-on-stream. Exemplary error bars are shown based on the reproduction of the reaction with different catalyst batches. If not shown, the deviation in the formate and acetate concentrations was below the accuracy of the HPLC method (±0.1 mM).

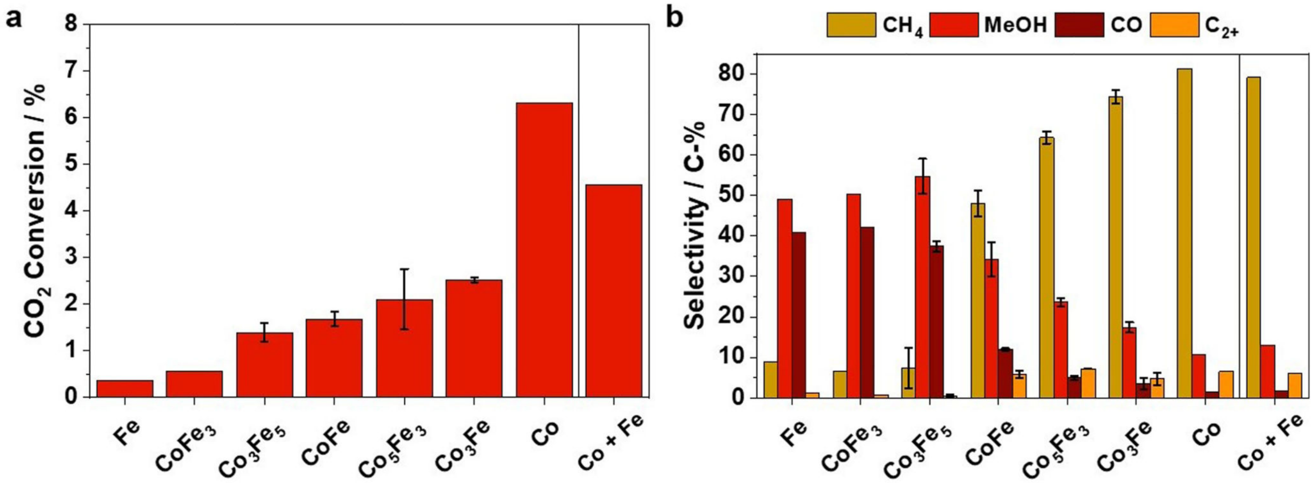

Figure 4.

(a) Catalytic activity and (b) product selectivity for CH_4, methanol, CO, and C_{2+} hydrocarbons determined by online GC after 54 h time-on-stream. Reaction conditions: T = 180 °C, p=2.0 MPa, $H_2/CO_2/Ar$=6:3:1, 4000 $cm^3\ h^{-1}\ g_{cat}^{-1}$. Exemplary error bars are shown based on the reproduction of the reaction with different catalyst batches.

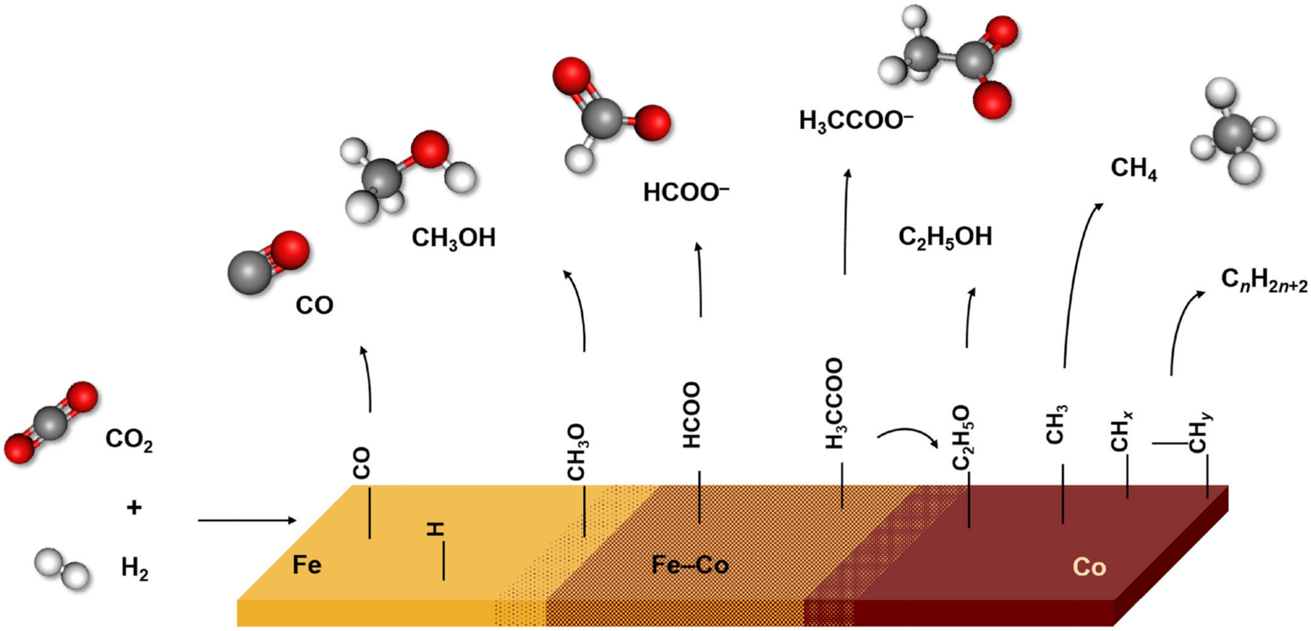

Figure 5.

Schematic representation of product formation in CO_2 reduction on silica-supported Fe-rich, Co-rich, and Co−Fe alloy catalysts. For simplicity the materials are presented without the silica support.

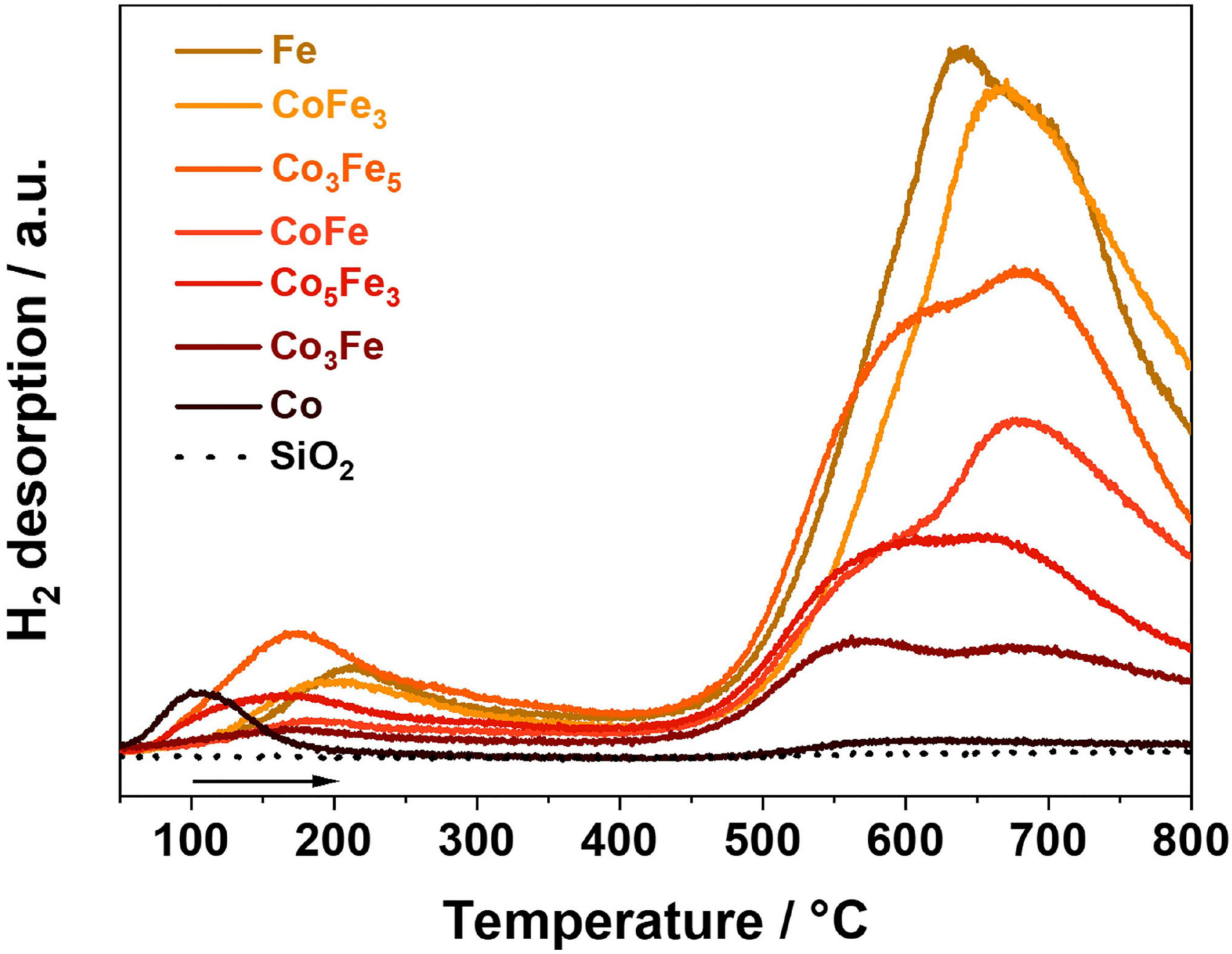

Figure 6. H_2-TPD profiles of silica-supported Co−Fe catalysts tracked by QMS at *m*/*z* = 2.

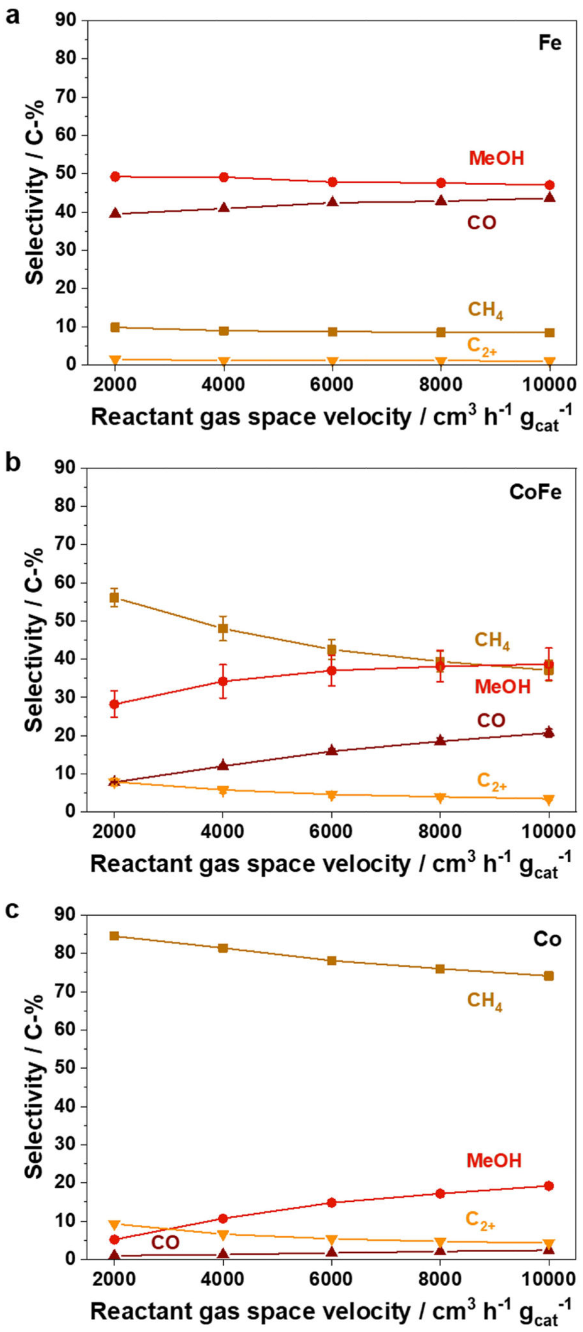

Figure 7.

Gas phase product selectivities as a function of the reactant gas space velocity ($H_2/CO_2/Ar$=6:3:1), defined as volume flow per hour and mass of catalyst, for silica-supported (a) Fe, (b) CoFe, and (c) Co. Reaction conditions: T=180 °C, p=2.0 MPa. Exemplary error bars are shown based on the reproduction of the reaction with different catalyst batches.

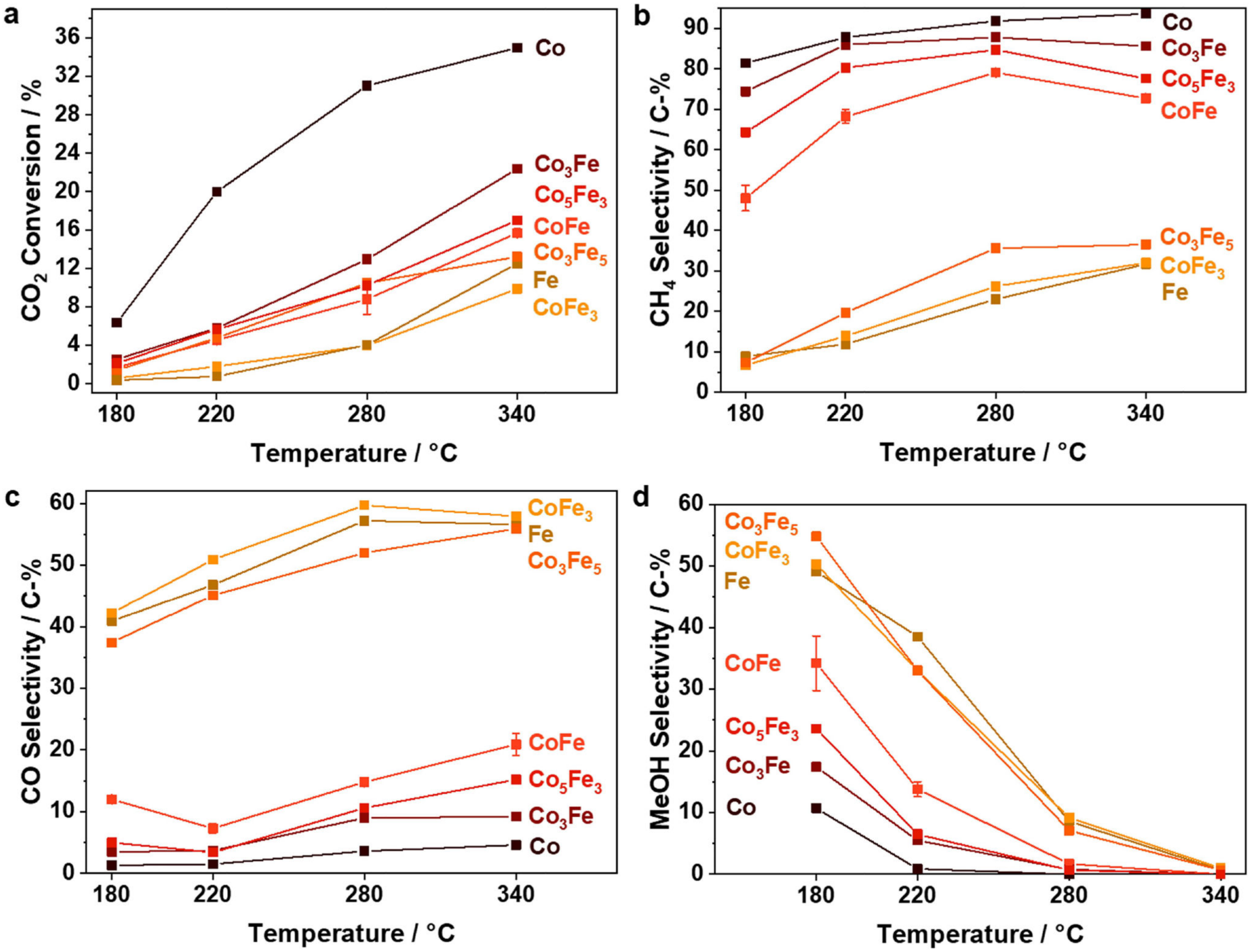

Figure 8.

(a) CO_2 conversions and **g**as phase product selectivities of (b) CH_4, (c) CO, and (d) methanol as a function of the reaction temperature. Reaction conditions: p=2.0 MPa, $H_2/CO_2/Ar$=6:3:1, 4000 cm^3 h^{-1} g_{cat}^{-1}. Exemplary error bars are shown based on the reproduction of the reaction with different catalyst batches.